



ORIGINAL ARTICLE

Endoplasmic reticulum-targetable selenium-doped carbon nanodots with redox-responsive fluorescence for in situ free-radical scavenging in cells and mice



Lei Yang^a, Hong Huang^c, Ting Wang^a, Danling Zhou^{a,*}, Qing Chen^b, Dan Li^b, Shuzi Chen^b, Ping Lin^{b,*}

^a School of Health & Social Care, Shanghai Urban Construction Vocational College, Shanghai 201415, China

^b Clinical Laboratory, Shanghai Mental Health Center, Shanghai 200030, China

^c College of Biological Chemical Sciences and Engineering, Jiaying University, Jiaying 314001, China

Received 6 December 2022; accepted 27 May 2023

Available online 2 June 2023

KEYWORDS

Endoplasmic reticulum;
Antioxidant;
Superoxide anion;
Hydroxyl radical;
Inflammation

Abstract Endoplasmic reticulum, the largest cellular organelle where protein synthesis, folding, transportation, and the maintenance of Ca^{2+} homeostasis occurred, is sensitive to the imbalance of its inner environment. Particularly, overproduction of reactive oxygen species in endoplasmic reticulum region can initiate endoplasmic reticulum stress and is tightly related to many metabolic diseases. In this respect, to retain normal function of endoplasmic reticulum, it is highly important to synthesize antioxidants with endoplasmic reticulum-targeting capability for precisely clearing excessively generated reactive oxygen species in endoplasmic reticulum. Herein, we demonstrate the preparation of endoplasmic reticulum-targeting Se-doped carbon nanodots and assays with HeLa cells as well as in vivo tests with mice have shown that the prepared carbon nanodots can significantly eliminate both $\bullet\text{OH}$ and $\text{O}_2^{\bullet-}$. Experimental results declared that the fabricated carbon nanodots with powerful scavenging capabilities toward $\bullet\text{OH}$ and $\text{O}_2^{\bullet-}$, low cytotoxicity and endoplasmic reticulum targetability can be utilized to protect cells against raised levels of reactive oxygen species in endoplasmic reticulum. What's more, the fabricated carbon nanodots effectively alleviated phorbol 12-myristate 13-acetate induced ear inflammation in live mice.

© 2023 The Author(s). Published by Elsevier B.V. on behalf of King Saud University. This is an open access article under the CC BY-NC-ND license (<http://creativecommons.org/licenses/by-nc-nd/4.0/>).

1. Introduction

Reactive oxygen species (ROS) comprised of oxygen radicals, such as superoxide ($\text{O}_2^{\bullet-}$) and hydroxyl radicals ($\bullet\text{OH}$), and nonradical oxidizing agents, such as hydrogen peroxide (H_2O_2), are a class of highly re-

active oxygen containing molecules (Hou et al., 2020; Li and Ma, 2018; Huang and Tian, 2018; Liu et al., 2022; Liu and Tian, 2021). In normal cellular environments, the amount of intracellular ROS is precisely regulated by enzymatic and nonenzymatic antioxidant system. The produced ROS are helpful to multiple critical biological processes, such as signal transduction, defense of pathogens invasion, and cell redox

* Corresponding authors.

E-mail addresses: zhoudanling@succ.edu.cn (D. Zhou), linpingsun2000@aliyun.com (P. Lin).

<https://doi.org/10.1016/j.arabjc.2023.105036>

1878-5352 © 2023 The Author(s). Published by Elsevier B.V. on behalf of King Saud University.

This is an open access article under the CC BY-NC-ND license (<http://creativecommons.org/licenses/by-nc-nd/4.0/>).

homeostasis (Zhen and Pu, 2018; Liu et al., 2023). However, under some conditions, such as anemia, long-term UV exposure or excessive intake of food additives, overproduction of ROS can occur and lead to oxidative stress and succeeding functional decline of biosystems, which are closely related to serious human diseases (Dickinson and Chang, 2011). As such, to retain normal function and prolong the lives of cells, it is of great importance to establish reliable and effective methodologies to diminish superfluous free radicals.

Until now, a series of antioxidants based on nanomaterials, including cerium oxide nanoparticles (Zhang et al., 2020); polydopamine nanoparticles (Bao et al., 2018); graphdiyne nanoparticles (Xie et al., 2020), iridium nanoparticles (Zhang et al., 2021), biopolymers (Zhang et al., 2020), metal-organic frameworks (Li et al., 2021), carbon nitride nanosheets (Cao et al., 2020), and carbon nanodots (CDs) (Luo et al., 2020; Das et al., 2014), have been reported for their medicinal effects to treat ROS related injury and/or diseases. Among them, CDs as a new type of zero-dimensional fluorescent carbonaceous nanomaterials have gained tremendous research interests in recent years because of their fascinating properties and have been widely used in biosensing (Zhou et al., 2017; Li et al., 2020; Huang et al., 2022); bioimaging (Zhao et al., 2020; Du et al., 2020), drug delivery (Wang et al., 2021), as well as antibacterial agents and antioxidants (Li et al., 2019; Zhou et al., 2021). For instance, Zhang et al. developed a benign approach to fabricate nitrogen and sulfur co-doped CDs for alleviating cellular oxidative stress (Zhang et al., 2018). Cai's group prepared selenium-doped CDs that possessing broad-spectrum antioxidant properties and renal specificity for acute kidney injury management (Rosenkrans et al., 2020). More recently, Chen and coworkers prepared tellurium-doped CDs that can consume intracellular ROS and protect cells against H₂O₂ (Chen et al., 2020). These reported CDs are conducive to blocking oxidative injuries from ROS and would facilitate the development of CD-based antioxidants for practical application in biomedical fields. As ROS show remarkably high reactivity and short half-life, it is desirable to synthesize antioxidants with targeting ability for scavenging ROS in situ, i.e., eliminating ROS right in the place where it is generated. Endoplasmic reticulum (ER), the largest cellular organelle where protein synthesis, folding, transportation, and the maintenance of Ca²⁺ homeostasis occurred, is sensitive to the imbalance of its inner environment (Wang and Kaufman, 2014; Deng et al., 2020). Particularly, excessive generation of ROS in ER can initiate ER-stress, which is closely related to many metabolic diseases, such as diabetes, obesity, and insulin resistance. In this context, to retain normal function of ER, it is critical to prepare antioxidants with ER-targeting capability for accurately clearing excessive ROS in the ER region.

To our knowledge, no ER-targeted antioxidants have yet been reported. To fill the gap, herein we demonstrate the preparation of ER-targeting Se-doped CDs (ER-Se-CDs) and assays with HeLa cells as well as in vivo tests with mice have shown that ER-Se-CDs can significantly eliminate both •OH and O₂⁻ (Fig. 1). Se-CDs covered with redox-responsive moiety (-C-Se) were conveniently prepared from selenocystamine through a benign hydrothermal approach, followed by the covalent conjugation with 3-((2-((4-methylphenyl)sulfonamido)ethyl)amino)-3-oxopropanoic acid, an ER targeting unit. The as-obtained ER-targeting unit modified Se-CDs, referred as ER-Se-CDs, showed superb scavenging capabilities toward O₂⁻ and •OH, low cytotoxicity, and ER targetability. By virtue of these properties, ER-Se-CDs had been resoundingly used to consume raised ROS in ER region. More excitedly, ER-Se-CDs can effectively relieve phorbol 12-myristate 13-acetate (PMA) triggered ear inflammation of live mice.

2. Experimental section

2.1. Reagents

Selenocystamine, 5,5-dimethyl-1-pyrroline N-oxide (DMPO), glutathione, riboflavin, methionine, nitro blue tetrazolium

(NBT), FeCl₂, NaHCO₃, H₂O₂ were supplied by Aladdin Chemistry Co. Ltd. N-(2-aminoethyl)-4-methyl-benzenesulfonamide, phorbol 12-myristate 13-acetate (PMA), 3-(4,5-dimethylthiazol-2-yl)-2,5-diphenyl tetrazolium bromide (MTT), and LiOH were bought from Sigma-Aldrich. Methyl 3-chloro-3-oxopropanoate was a kind gift from Dr. Zhichao Liu. 2',7'-Dichlorofluorescein diacetate (DCFH-DA) were purchased from Beyotime Chemical Reagent Co. Ltd. High glucose Dulbecco's modified Eagle's media (DMEM) were received from KeyGEN Biotech. Co. Ltd. All the mentioned reagents were of analytical grade and used as received.

2.2. Characterizations

Absorption spectra were acquired on a Shimadzu UV-2550 spectrophotometer. Fluorescence spectra were measured on a F-4600 fluorescence spectrophotometer (Hitachi). Transmission electron microscopy (TEM) experiments were performed on transmission electron microscope working at an acceleration voltage of 200 kV (JEOL JEM-2100F). Atomic force microscopic (AFM) characterizations were conducted in the ScanAsyst mode under ambient conditions (Bruker). X-ray photoelectron spectroscopy (XPS) data was collected using a thermolectron instrument (Thermo Scientific ESCALAB 250). Fourier transform infrared spectroscopy (FTIR) spectrum of the samples were acquired by applying a Nicolet iS10 FTIR spectrometer. Electron spin resonance (ESR) experiments were carried out on a Bruker ELEXSYS E500 ESR spectrometer. ¹H and ¹³C nuclear magnetic resonance (NMR) spectra were obtained from a Bruker 500 MHz spectrometer. Confocal fluorescence and bright field images (512 × 512 pixels) were acquired with a Leica TCS-SP8 confocal laser scanning microscope. Cells images were captured using a 63 × objective lens.

2.3. Synthesis of Se-CDs

Se-CDs can be synthesized from selenocystamine via a benign, one-pot solvothermal carbonization approach. Briefly, 0.1 g selenocystamine was dissolved in 40 mL of deionized water under rapid stirring. Then, the aqueous dispersion was transferred into a Teflon-lined autoclave (50 mL) and heated for 2 h at a temperature of 200 °C. The resulting solution with reddish brown color was filtrated with a 0.22 μm filter membrane, centrifugated at 12000 g for 10 min, and dialyzed through a dialysis tubing with a molecular weight cutoff of 1000 Da (changing the water every 8 h). After lyophilization of the purified solution, Se-CDs powder can thus be acquired.

2.4. Synthesis of 3-((2-((4-methylphenyl)sulfonamido)ethyl)amino)-3-oxopropanoic acid (abbreviated as MOA)

To a round-bottomed flask (100 mL), in which N-(2-aminoethyl)-4-methyl-benzenesulfonamide (1.0 g, 4.7 mmol) was dissolved into a mixed solution of tetrahydrofuran (20 mL) and saturated NaHCO₃ solution (5 mL), was introduced methyl 3-chloro-3-oxopropanoate (0.7 g, 5.1 mmol). After reaction for 1 h at 0 °C, LiOH solution (2 M, 5 mL) was slowly injected, followed by another incubation at room temperature for ~12 h. Afterwards, the solvent was discarded under reduced pressure and the obtained residue was purified by HPLC

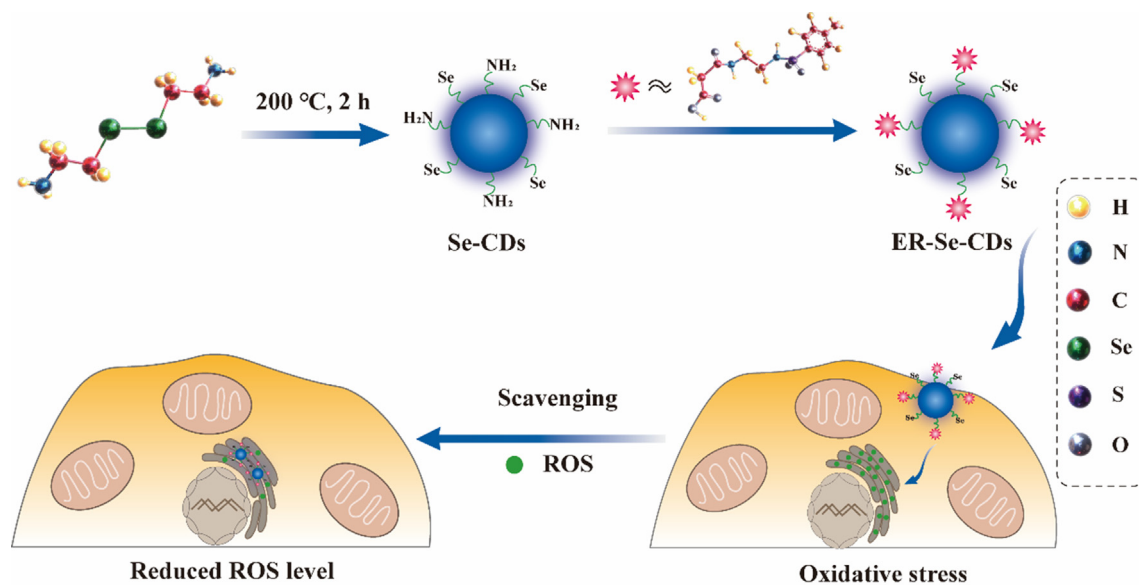


Fig. 1 Schematic illustration of the preparation of ER-Se-CDs and its utilization in diminishing ROS in ER.

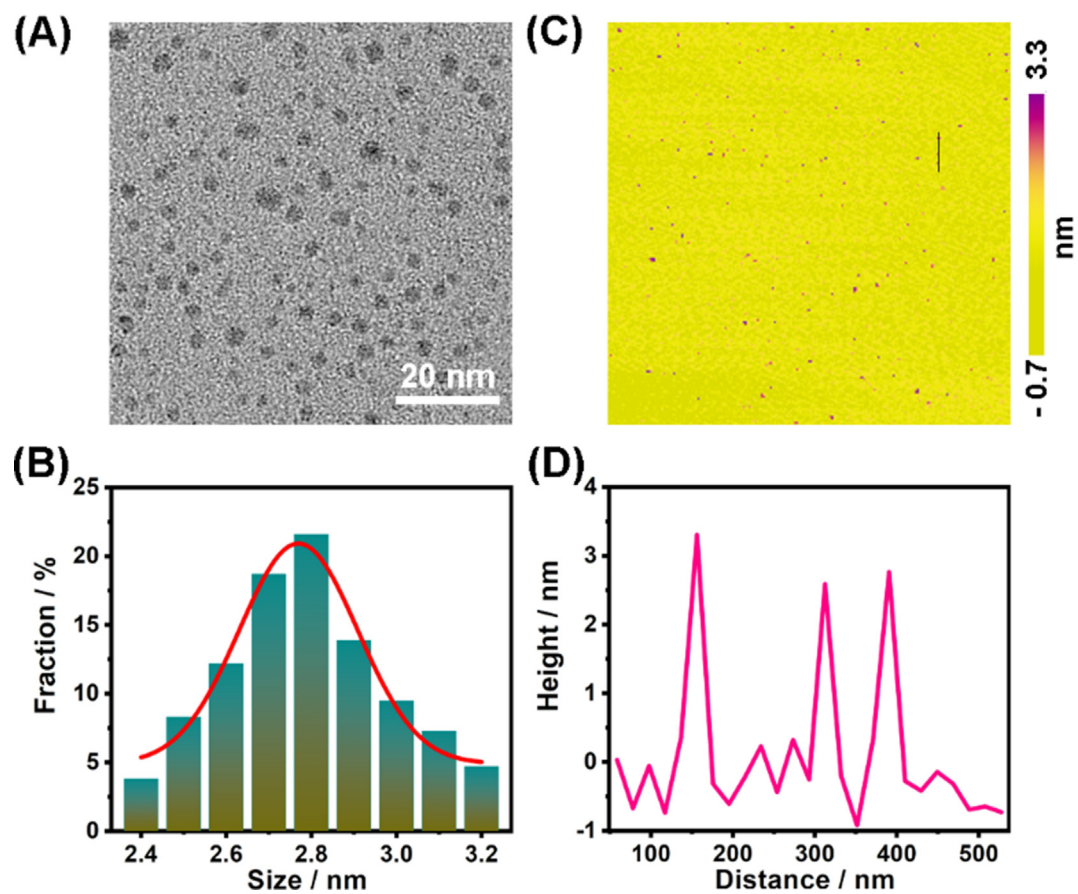


Fig. 2 (A) TEM characterization of Se-CDs. (B) Size distribution of Se-CDs. (C) Typical AFM image of Se-CDs. (D) Height distribution of Se-CDs along the black line in panel C.

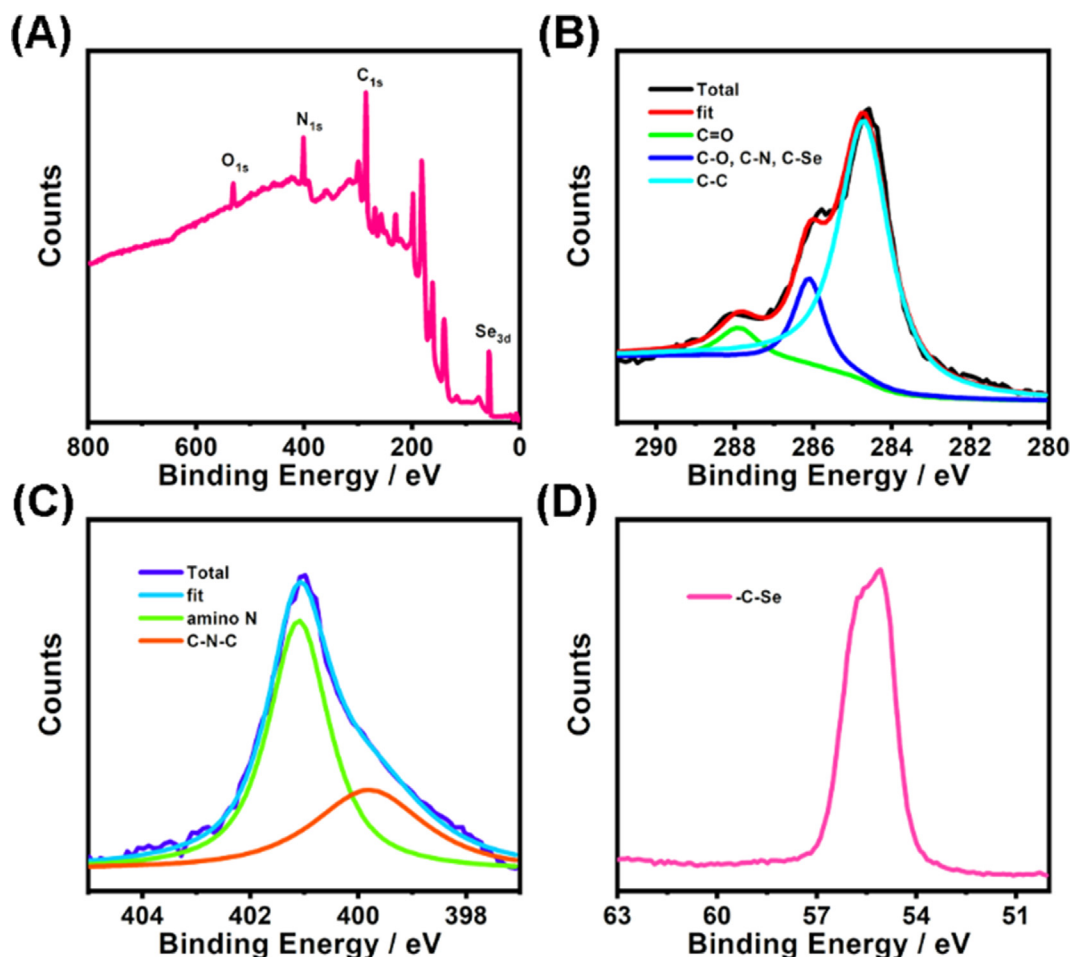


Fig. 3 (A) XPS survey spectrum of Se-CDs. (B) High-resolution C1s spectrum of Se-CDs. (C) High-resolution N1s spectrum of Se-CDs. (D) High-resolution Se3d spectrum of Se-CDs.

system using a gradient program (mobile phase: acetonitrile to water, from 5% to 95%, with 0.1% TFA) at 20 mL/min flow rate to afford desired product as pale yellow oily matter (0.24 g, yield: 17%). ^1H NMR (400 MHz, CDCl_3) δ (ppm): 7.92 (s, 1H), 7.77 (s, 1H), 7.67 (d, 2H), 7.22 (d, 2H), 6.31 (s, 1H), 3.37 (m, 4H), 3.00 (s, 2H), 2.34 (s, 3H). ^{13}C NMR (400 MHz, CDCl_3) δ (ppm): 171.11, 169.13, 143.63, 136.36, 129.82, 126.99, 42.16, 40.36, 39.66, 21.46. HRMS-ESI (m/z): $[\text{M} + \text{Na}]^+$ calcd for $\text{C}_{12}\text{H}_{16}\text{N}_2\text{NaO}_5\text{S}$: 323.0678; found: 323.0672.

2.5. Preparation of ER-Se-CDs

The immobilization of MOA on Se-CD's surface was realized under the activation of EDC/NHS. Typically, MOA solution (1.0 mL, 1.5 mM) was mixed with EDC/NHS (50 mg/50 mg) and activated at room temperature for 2 h. After then, Se-CDs solution (2.0 mL, $1.0 \text{ mg}\cdot\text{mL}^{-1}$) was introduced, and further reacted for one night to afford MOA functionalized Se-CDs (ER-Se-CDs). The unreacted MOA was removed by dialysis. By measuring the absorption spectra of MOA in the above collected water and the stock solution, density of MOA on the Se-CD surface were determined to be $46.6 \mu\text{mol}\cdot\text{g}^{-1}$.

2.6. Cytotoxicity evaluations

HeLa cells were fostered at a density of $\sim 1 \times 10^4$ cells per well in 96-well plates, and grown in DMEM containing 10% fetal bovine serum, $80 \text{ U}\cdot\text{mL}^{-1}$ penicillin, and $80 \mu\text{g}\cdot\text{mL}^{-1}$ streptomycin in a humid incubator with 5% $\text{CO}_2/95\%$ air. After 12 h, the culture media were removed, and fresh one with serial dilutions of ER-Se-CDs ($0\text{--}80 \mu\text{g}\cdot\text{mL}^{-1}$) was introduced, cultured for 48 h. As to each amount, five independent experiments were carried out. Thereafter, MTT solution ($1.0 \text{ mg}\cdot\text{mL}^{-1}$) with a volume of $20 \mu\text{L}$ was injected into each well, culturing for 4 h to allow the formation of formazan crystals. Subsequently, $150 \mu\text{L}$ DMSO was added into the wells. Absorbance (A) of the resultant hybrid at 570 nm was measured. Cellular viability values were counted according to the following equation: cellular viability (%) = $A_{\text{test}}/A_{\text{control}} \times 100\%$, where A_{control} refers to the absorbance recorded from the control group, and A_{test} refers to the absorbance obtained with the presence of ER-Se-CDs.

2.7. Cellular imaging

The subcellular localization of ER-Se-CDs was investigated by co-localization bioimaging experiment, in which ER-Se-CDs

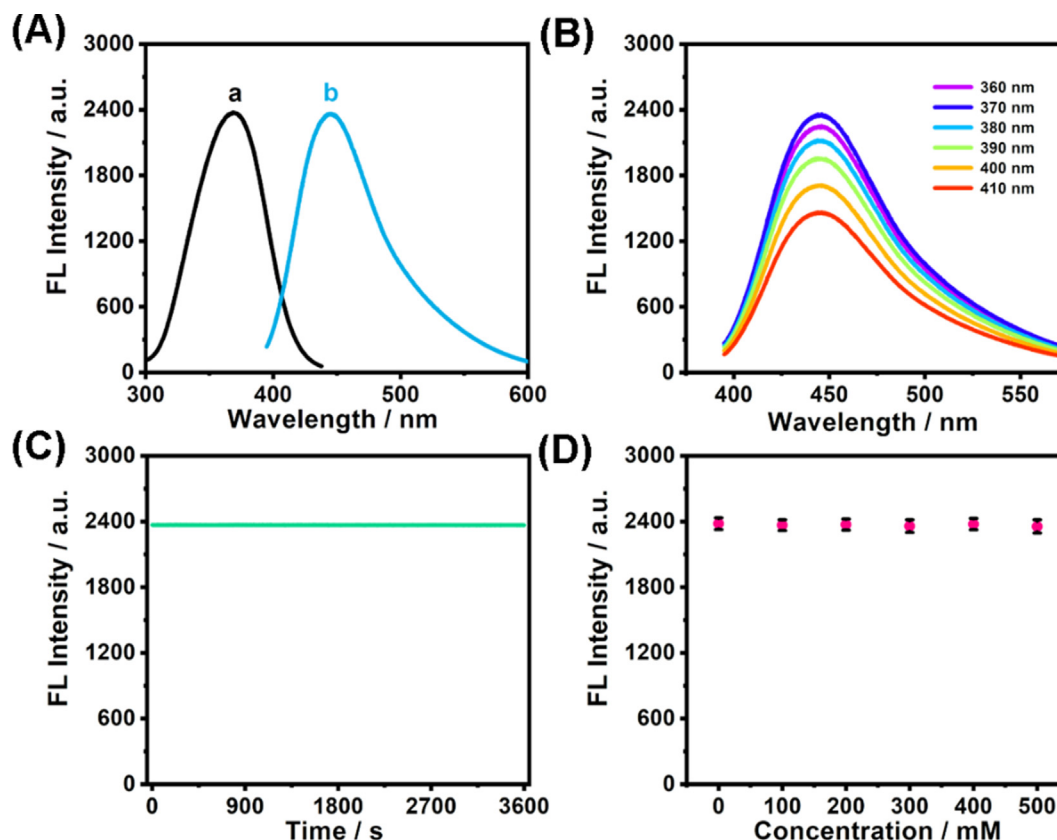


Fig. 4 (A) Fluorescence spectra of Se-CDs (a: excitation spectrum; b: emission spectrum). (B) Fluorescence spectra of Se-CDs gained at varied excitation from 360 to 410 nm. (C) Change of fluorescence intensity under uninterrupted irradiation by a 90 W Xe lamp ($\lambda_{\text{ex}} = 405$ nm). (D). Variation of fluorescence intensity at 445 nm in NaCl solution.

($20 \mu\text{g}\cdot\text{mL}^{-1}$) stained cells were again stained for 20 min with ER-Tracker Red (50 nM). After finishing the labeling experiments, cells were rinsed thoroughly with cool PBS. Fluorescence signal of ER-Tracker Red was obtained in 570–650 nm wavelength region (excited at 552 nm), as for ER-Se-CDs, an excitation wavelength of 405 nm was selected, and its blue fluorescence was collected in the wavelength region of 410–480 nm.

2.8. In vivo imaging

All animal experiments were approved by the Animal Ethics Committee of East China Normal University. Kunming male mice with a body weight of 15 g were selected for establishing an ear inflammation model, which was triggered by topically applying PMA solution ($100 \mu\text{g}\cdot\text{mL}^{-1}$, 50 μL) on the right ear. After incubation for 6 h, the mice were subcutaneously administered with ER-Se-CDs ($20 \mu\text{g}\cdot\text{mL}^{-1}$, 100 μL ; $40 \mu\text{g}\cdot\text{mL}^{-1}$, 100 μL). 0.5 h later, DCFH-DA (1 mM, 50 μL), a non-fluorescent cell permeable dye that reacts with intracellular ROS and emits fluorescence at 520 nm was injected. After another 0.5 h, fluorescence image of the mice body was captured with a PerkinElmer in vivo imaging system ($\lambda_{\text{ex}} = 488$ nm; $\lambda_{\text{em}} = 520$ nm).

3. Results and discussion

3.1. Characterization of Se-CDs

In our experiment, Se-CDs can be conveniently prepared by one-step hydrothermal treating of selenocystamine solution (Fig. 1). The size and morphology of the obtained Se-CDs were characterized by TEM and AFM. TEM image in Fig. 2A shows that Se-CDs are distributed randomly and uniformly with a narrow size distribution in 2.4 ~ 3.2 nm range (Fig. 2B). This size is comparable to other heteroatom doped CDs (Gong et al., 2016; Liu et al., 2017). The morphology of Se-CDs was further examined by AFM (Fig. 2C). From which, we can see that Se-CDs were monodispersed. The line scan of three individual CDs reveals that their topographic heights range from 2.6 to 3.3 nm (Fig. 2D), which agrees well with the TEM characterization.

Then, functional groups of the Se-CDs were studied by XPS experiments. As depicted in the XPS survey spectrum (Fig. 3A), four main peaks were found at 530.8 eV (O_{1s}), 399.8 eV (N_{1s}), 284.7 eV (C_{1s}), along with 55.1 eV (Se_{3d}), demonstrating that Se-CDs are dominantly composed of oxygen (atomic ratio: 9.57%), nitrogen (18.62%), carbon (64.91%), and selenium (6.9%). Deconvoluted XPS spectra

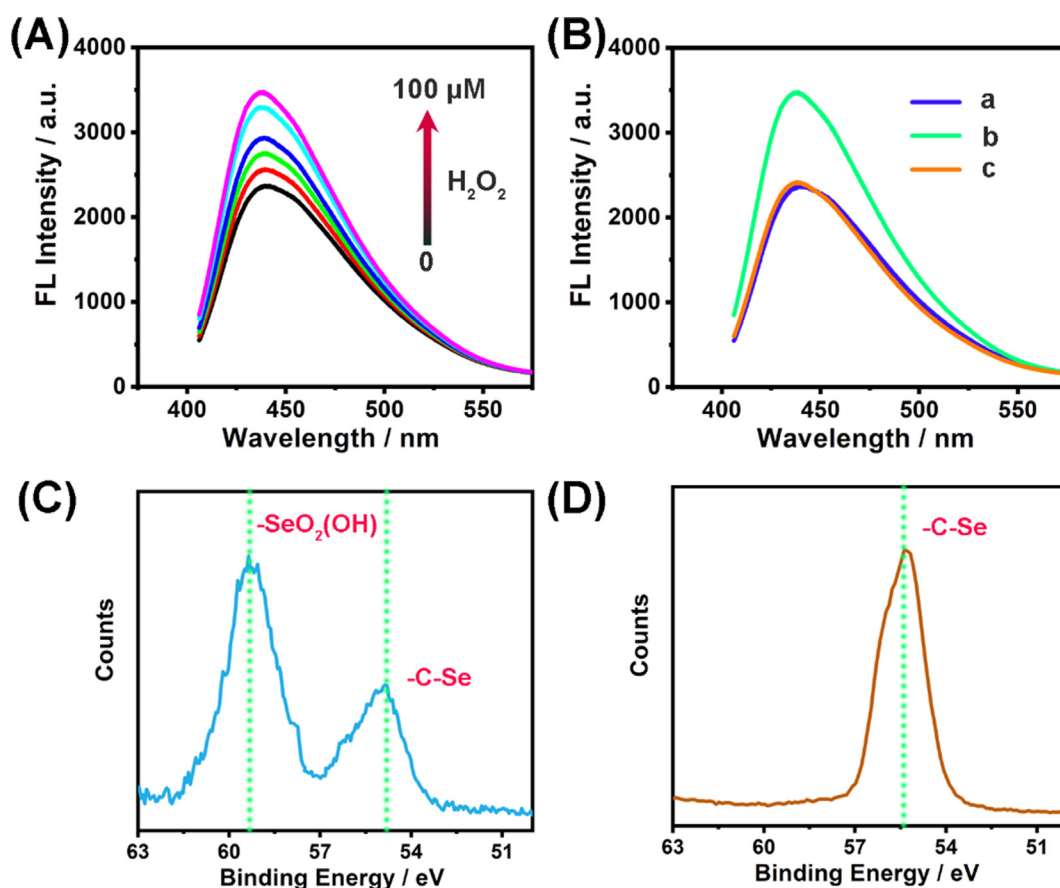


Fig. 5 (A) Fluorescence response of Se-CDs ($20 \mu\text{g}\cdot\text{mL}^{-1}$) to various amounts of H_2O_2 (From bottom to up: 0, 20, 40, 60, 80, and $100 \mu\text{M}$). (B) Redox-responsive fluorescence of Se-CDs: (a) Se-CDs ($20 \mu\text{g mL}^{-1}$); (b) Se-CDs ($20 \mu\text{g mL}^{-1}$) + H_2O_2 ($100 \mu\text{M}$); (c) Se-CDs ($20 \mu\text{g mL}^{-1}$) + H_2O_2 ($100 \mu\text{M}$) + glutathione (1.0 mM). (C) High-resolution XPS spectrum of Se_{3d} in Se-CDs reacted with H_2O_2 . (D) High-resolution XPS spectrum of Se_{3d} in Se-CDs reacted with H_2O_2 and glutathione.

for C_{1s} (Fig. 3B) show that the C_{1s} band contains three distinct peaks at 284.7, 286.1, and 287.9 eV, attributed to C–C, C–N/C–O/C–Se, and C = O, respectively (Li et al., 2017; Liu et al., 2020; Liu et al., 2023). Deconvoluted XPS spectra for N_{1s} spectra show two peaks at 399.8 and 401.1 eV, ascribed to C–N–C and amino N, respectively (Fig. 3C) (Lu et al., 2017; Zhao et al., 2021). The high-resolution XPS spectrum of Se_{3d} (55.1 eV) reveals –C–Se group existed on the surface of Se-CDs (Fig. 3D) (Huang et al., 2020). Besides, the absorption peaks appeared in the FTIR spectrum at 3429, 1578, and 1221 cm^{-1} , respectively corresponding to N–H, C = N, and C–N, which suggested the existence of amine groups on the surface of the Se-CDs (Figure S1, curve a) (Gong et al., 2019).

Subsequently, the optical features of Se-CDs were monitored. The absorption spectrum of Se-CDs presents two peaks at 241 and 299 nm, as indicated in Figure S2, which respectively attributes to the $\pi\text{-}\pi^*$ transition of C = C band and $n\text{-}\pi^*$ electron transition of C = O band (Lu et al., 2018; Wang et al., 2016; Li et al., 2018). Under the excitation with a maximum wavelength of 369 nm (Fig. 4A, curve a), a strong emission peak centered at 445 nm is observable (Fig. 4A, curve b). Using quinine sulfate in 0.10 M H_2SO_4 solution as the reference, fluorescence quantum yield of Se-CDs was calculated to be 8.3%, which is comparable to Se-CDs reported by Xu

and coworkers (Li et al., 2017). However, unlike previously reported Se-CDs, which show excitation-energy dependent fluorescence, the fluorescence peak of Se-CDs did not change under excitation in the wavelength range from 360 to 410 nm (Fig. 4B). The excitation-energy independent fluorescence of our Se-CDs probably result from its uniform size (Wang and Hu, 2014; Li et al., 2010). Remarkably, Se-CDs had robust photostability. Illuminating Se-CDs with a 405 nm light for 1 h witnessed truly little variation of its fluorescence (Fig. 4C). Besides, there were no changes in fluorescence intensity at high ionic strengths (Fig. 4D), suggesting the great potency of Se-CDs to be used in physical salt concentrations.

Moreover, we found Se-CDs exhibited redox-responsive fluorescence. As shown in Fig. 5A and Fig. 5B (curve a and curve b), addition of H_2O_2 to Se-CD solution could induce an apparent increment of its fluorescence. At the same time, selenic acid was generated in the presence of H_2O_2 (Fig. 5C). However, when reduced glutathione was introduced into the above mixed solution of Se-CDs and H_2O_2 , the fluorescence intensity was nearly reduced back to its initial state (Fig. 5B, curve c). Concurrently, –C–Se was generated from the reduction of selenic acid (Fig. 5D). Overall, these analyses suggested that the redox state of Se atom had a prominent influence on the fluorescence of Se-CDs.

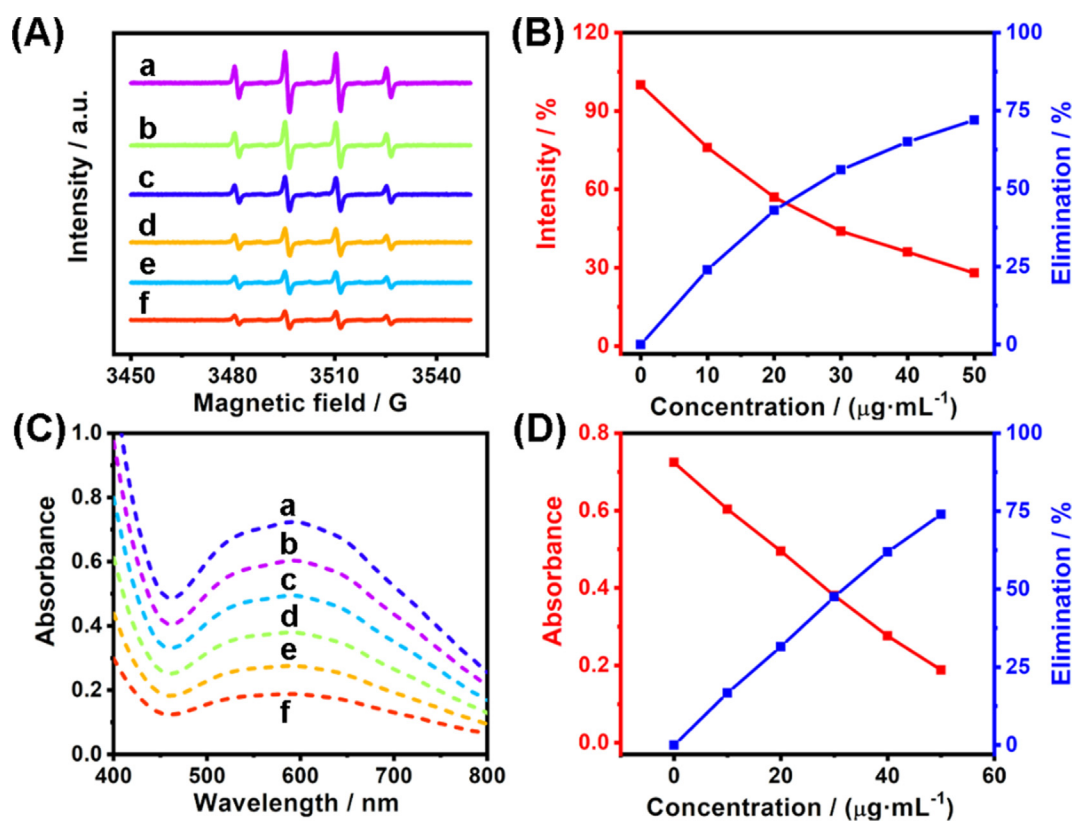


Fig. 6 (A) ESR spectra of DMPO (50 mM) with the co-existence of •OH (10 μM) and different amounts of ER-Se-CDs (a: 0 μg·mL⁻¹; b: 10 μg·mL⁻¹; c: 20 μg·mL⁻¹; d: 30 μg·mL⁻¹; e: 40 μg·mL⁻¹; f: 50 μg·mL⁻¹). (B) The corresponding intensity of ESR signal and elimination efficiency of ER-Se-CDs toward •OH. (C) Absorption spectra of a system comprised of riboflavin, methionine, and NBT with the existence of different concentrations of ER-Se-CDs (a: 0 μg·mL⁻¹; b: 10 μg·mL⁻¹; c: 20 μg·mL⁻¹; d: 30 μg·mL⁻¹; e: 40 μg·mL⁻¹; f: 50 μg·mL⁻¹). (D) The corresponding absorbance and elimination efficiency of ER-Se-CDs toward O₂^{•-}.

3.2. Synthesis of ER-Se-CDs

We then synthesized an ER targeting molecule, MOA, whose chemical structure was verified by ¹H NMR, ¹³C NMR, and HRMS (Figure S3–S6). MOA was rationally designed with two functional moieties. Moiety one is a methyl sulphonamide group, which is commonly used for targeting molecules and/or nanomaterials into ER region (Xiao et al., 2018; Huang et al., 2022), and moiety two is a carboxyl group that can be used for further conjugation with amine group. The fixation of MOA on Se-CDs was affirmed by FTIR spectroscopy. As shown in Fig. S1 (curve c), an absorption band at 1153 cm⁻¹, assigned to the C-S group in MOA, was found in the FTIR spectrum of ER-Se-CDs. Additionally, a larger hydrodynamic size was obtained for ER-Se-CDs, as compared with that of Se-CDs, which further testified the successful preparation of ER-Se-CDs (Figure S7). It is worthy to note that the attachment of MOA on Se-CDs had no obvious influence on the size and fluorescence of Se-CDs (Figure S8–S9).

3.3. ROS scavenging efficiency of ER-Se-CDs

The existence of redox-responsive unit -C-Se on the surface of ER-Se-CDs implied its possibility to be used for eliminating •OH and O₂^{•-}. For investigating its elimination efficiency to-

ward •OH, ESR experiments, a direct and reliable method to detect ROS, were carried out, in which Fe²⁺/H₂O₂ was chosen as the source to provide •OH and 5,5-dimethyl-1-pyrroline N-oxide (DMPO) as the spin trap agent (Huang et al., 2019). Typically, an intense four-line ESR signal with a height ratio of 1:2:2:1, characteristic of DMPO-OH adduct, could be detected once Fe²⁺/H₂O₂ was injected to DMPO solution, evidencing the high level of •OH (Fig. 5A, curve a). Upon ER-Se-CDs treatment, the ESR intensity of the above mixture significantly weakened in a dose-dependent manner (Fig. 6A, curve b-f). The ESR signal intensity decreased down to 28.1% (elimination efficiency: 71.9%) with the involvement of ER-Se-CDs at a concentration of 50 μg·mL⁻¹ (Fig. 6B), indicating ER-Se-CDs possessed an excellent removal capacity toward •OH. Subsequently, O₂^{•-} removal capacity was assessed through determining the inhibition ratio of NBT reduction by O₂^{•-}. As seen in Fig. 6C (curve a), a strong absorption signal around 560 nm appeared after photoirradiation (intensity: 3500 lx; irradiation time: 15 min) of a mixture containing methionine, riboflavin, and NBT, reflecting the generation of O₂^{•-} in this process (Zhang et al., 2021). Once ER-Se-CDs was added into the aforesaid mixture, the absorption signal significantly decreased (Fig. 6C, curve b-f), as expected. More than 70% O₂^{•-} could be removed from the solution with ER-Se-CDs treatment at the concentration of 50 μg·mL⁻¹ (Fig. 6D), sug-

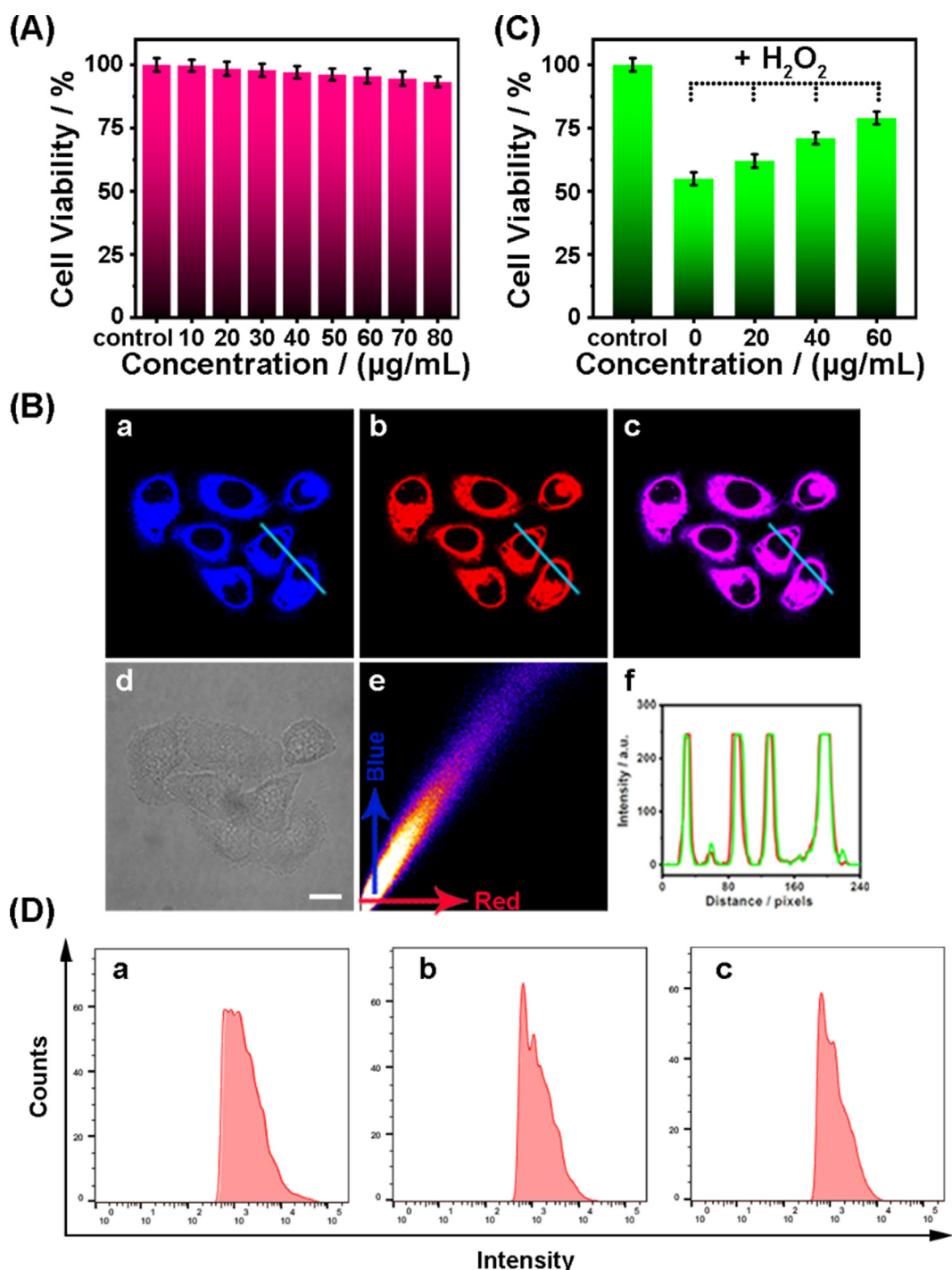


Fig. 7 (A) Viabilities of HeLa cells incubated with different amounts of ER-Se-CDs. (B) Co-localization investigations in HeLa cells that were co-labeled with ER-Se-CDs ($20 \mu\text{g}\cdot\text{mL}^{-1}$) and ER-Tracker Red (50 nM): (a) fluorescence image from ER-Se-CDs ($\lambda_{\text{em}} = 410\text{--}480 \text{ nm}$, $\lambda_{\text{ex}} = 405 \text{ nm}$); (b) fluorescence image from ER-Tracker Red ($\lambda_{\text{em}} = 570\text{--}650 \text{ nm}$, $\lambda_{\text{ex}} = 552 \text{ nm}$); (c) the merged image of (a) and (b); (d) the bright field image; (e) the corresponding intensity correlation plot of the blue channel with red channel; (f) intensity profiles of ER-Se-CDs and ER-Tracker Red along the line across the cell. Scale bar: $10 \mu\text{m}$. (C) Protective capabilities of ER-Se-CDs to HeLa cells from oxidative damage initiated by H_2O_2 ($150 \mu\text{M}$). Data showed are mean values and standard deviations from five independent experiments. (D) HeLa cells were co-incubated with DCFH-DA ($10 \mu\text{M}$) and PMA ($3 \mu\text{g}\cdot\text{mL}^{-1}$) with or without ER-Se-CDs and analyzed by flow cytometry: (a) DCFH-DA + PMA; (b) DCFH-DA + PMA + ER-Se-CDs ($20 \mu\text{g mL}^{-1}$); (c) DCFH-DA + PMA + ER-Se-CDs ($40 \mu\text{g}\cdot\text{mL}^{-1}$).

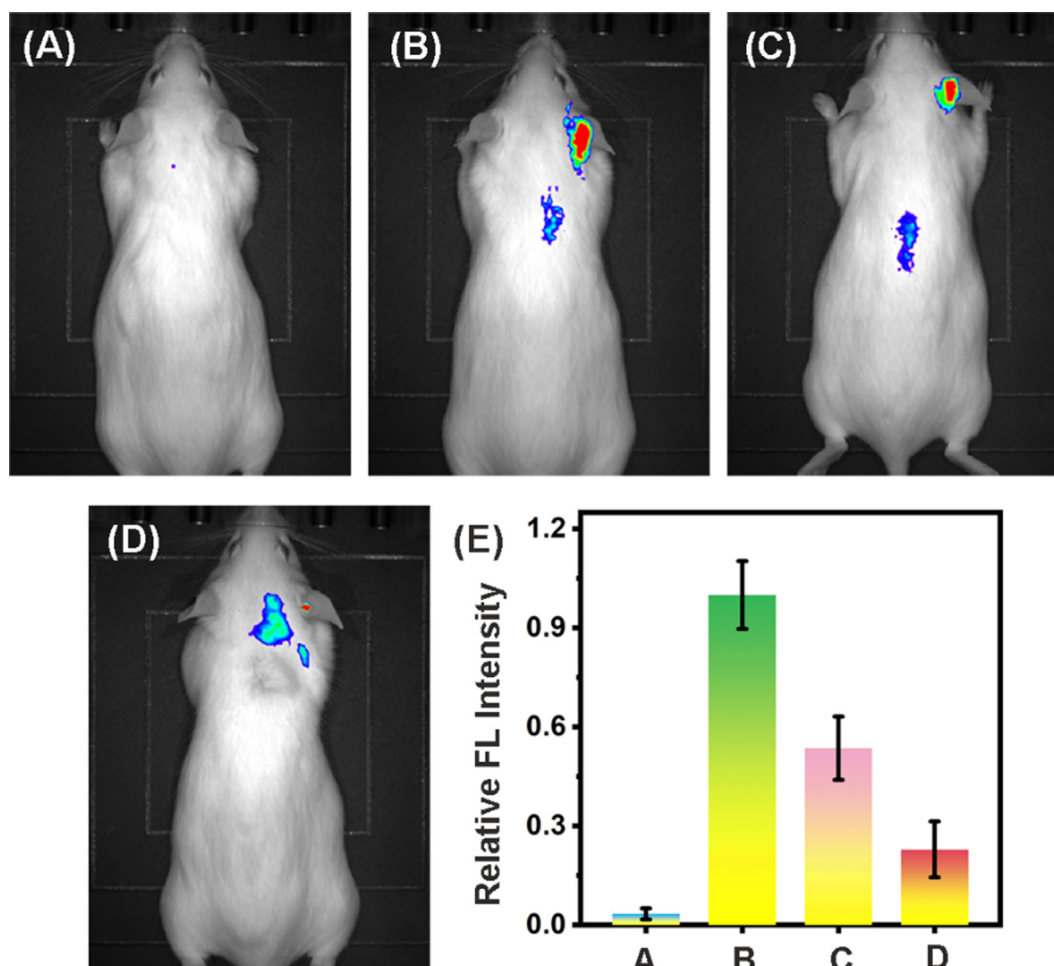


Fig. 8 (A) In vivo fluorescence imaging of mouse solely treated with DCFH-DA (1 mM, 50 μ L) in the right ear region. (B) In vivo fluorescence imaging of mouse sequentially treatment with PMA (100 μ g·mL⁻¹, 50 μ L) and DCFH-DA (1 mM, 50 μ L). (C) In vivo fluorescence imaging of mouse orderly treated with PMA (100 μ g·mL⁻¹, 50 μ L), ER-Se-CDs (20 μ g·mL⁻¹, 100 μ L), and DCFH-DA (1 mM, 50 μ L). (D) In vivo fluorescence imaging of mice sequentially treated with PMA (100 μ g·mL⁻¹, 50 μ L), ER-Se-CDs (40 μ g·mL⁻¹, 100 μ L), and DCFH-DA (1 mM, 50 μ L). Each group contains five mice. (E) Relative fluorescence intensity in panel A–D. All the fluorescence intensities were compared to panel B, which was normalized to 1.0.

gesting the forceful $O_2^{\cdot-}$ removing ability of ER-Se-CDs. These results demonstrated that ER-Se-CDs can act as efficient scavengers for both $\bullet OH$ and $O_2^{\cdot-}$.

3.4. Scavenging activity of ER-Se-CDs in cells

After successfully verifying ER-Se-CDs' antioxidant capacity, its potency as scavengers against intracellular ROS was explored. Prior to this investigation, cytotoxicity of ER-Se-CDs was studied by standard MTT assay with various dosages of ER-Se-CDs and incubated for a period of 48 h. The findings, as shown in Fig. 7A, revealed that even incubated with a high dosage (up to 80 μ g·mL⁻¹) of ER-Se-CDs, the cells still showed a high viability rate over 90%. As such, we conclude that ER-Se-CDs is almost nontoxic to live cells.

As ER-Se-CDs was functionalized by methyl sulphonamide group, which possesses ER-targeting capability, we then examined its potential to localize into ER of cells. In this respect, co-localization experiment was conducted via treating cells with ER-Se-CDs (20 μ g·mL⁻¹) and commercial ER-Tracker Red

(50 nM) in sequence. As displayed in Fig. 7B, the bright blue fluorescence from ER-Se-CDs (Fig. 7Ba) showed a large extent of overlap with the red fluorescence from ER-Tracker Red (Fig. 7Bb), as observed from the intense pink signal in the merged image (Fig. 7Bc). The corresponding Pearson's coefficient is 0.87 (Fig. 7Be). Moreover, the variations in the intensity profiles of the lines across the cells are coinstantaneous in the two separate channels (Fig. 7Bf). On the other hand, a high Pearson's coefficient value of 0.85 was also obtained when co-localization experiments were conducted in living astrocytes with ER-Se-CDs and ER-Tracker Red (Fig. S10). These results inferred that with the anchor of methyl sulphonamide group, ER-Se-CDs, as expected, can selectively reside in ER region.

Oxidative stress occurs as the amount of ROS exceeds the antioxidant competence of cellular antioxidants, giving rise to severe harm to nucleic acids, proteins, and lipids. Since ER-Se-CDs presented high elimination efficiency toward $\bullet OH$ and $O_2^{\cdot-}$, low cytotoxicity, and ER targetability, we envisioned that ER-Se-CDs could exert an efficient protection against ROS-induced damage within ER. Then, H_2O_2 was served as

the damage initiator to assess the protection ability of ER-Se-CDs against oxidative stress. The corresponding data are displayed in Fig. 7C. It was obvious that ER-Se-CDs, the first ER targetable nanoantioxidant, could dose-dependently restrain ROS-caused decline of cell viabilities. Moreover, to further monitor the cellular ROS level after treatment with different amounts of ER-Se-CDs, DCFH-DA assay was performed by flow cytometry. DCFH-DA itself showed no fluorescence. Once it enters into cells, it would be hydrolyzed by cellular enzyme to produce DCFH, which could emit strong fluorescence after being oxidized by ROS (Wei et al., 2019). As seen in Fig. 7D, a lower fluorescence intensity was observed for the cells pre-incubated with ER-Se-CDs than the cells treated with H₂O₂ alone, suggesting a lower level of ROS in the cells pre-treated with ER-Se-CDs. Together, these data demonstrate that ER-Se-CDs is competent to consume ROS in ER region.

3.5. *In vivo* anti-inflammation

The *in vivo* anti-inflammation performance of ER-Se-CDs was also studied. In the experiments, to establish an inflammation model of the right ear, PMA, an apoptotic drug that can initiate tissue inflammation was regionally applied. As shown, no visible fluorescence signal was found from the right ear of the mouse solely treated with DCFH-DA, manifesting a low level of ROS (Fig. 8A). In sharp contrast, a strong fluorescence was clearly perceptible from DCFH-DA and PMA co-treated ear, demonstrating the elevation of ROS level in this process (Fig. 8B). After subcutaneously treated with ER-Se-CDs, the fluorescence in the inflamed region strongly quenched (Fig. 8C and 8D). Additionally, as shown in Figure S11, hematoxylin and eosin (H&E) stained histological images of heart, liver, spleen, lung, and kidney demonstrated negligible toxicity of ER-Se-CDs toward major organs. These results indicated that ER-Se-CDs possessed an efficient ROS scavenging ability against ear inflammation in live mice with great biosafety.

4. Conclusion

In this work, we successfully constructed an ER-targeting Se-CDs that effectively eliminate both •OH and O₂^{•-} *in vitro* and *in vivo*. The Se-CDs with uniform size distribution and redox-responsive fluorescence can be conveniently synthesized via a one-pot hydrothermal method. After modified by methyl sulphonamide group, ER-Se-CDs with robust scavenging power toward •OH and O₂^{•-}, low cytotoxicity and ER targeting capability was obtained. Because of these satisfying properties, ER-Se-CDs had been utilized to protect cells against raised ROS levels in ER region. Importantly, ER-Se-CDs effectively relieved PMA-induced ear inflammation of live mice. To conclude, these results demonstrate that ER-Se-CDs is a promising nanoantioxidant for alleviating ROS-related inflammation and holds great prospect in clinic.

Declaration of Competing Interest

The authors declare that they have no known competing financial interests or personal relationships that could have appeared to influence the work reported in this paper.

Acknowledgements

The authors gratefully thank the Zhejiang Provincial Natural Science Foundation of China (Grant No. LQ20B050003), the

Scientific Research Project of Shanghai Urban Construction Vocational College (AA-05-2023-01-03-08; AA-05-2023-01-03-05-11).

Appendix A. Supplementary data

Supplementary data to this article can be found online at <https://doi.org/10.1016/j.arabjc.2023.105036>.

References

- Bao, X., Zhao, J., Sun, J., Hu, M., Yang, X., 2018. Polydopamine nanoparticles as efficient scavengers for reactive oxygen species in periodontal disease. *ACS Nano* 12, 8882–8892.
- Cao, X.-N., Lian, S., Tong, Y., Lin, W., Jia, L., Fang, Y., Wang, X., 2020. Fluorescent Se-modified carbon nitride nanosheets as biomimetic catalase for free-radical scavenging. *Chem. Commun.* 56, 916–919.
- Chen, H., Wen, K., Chen, J., Xing, W., Wu, X., Shi, Q., Peng, A., Huang, H., 2020. Ultra-stable tellurium-doped carbon quantum dots for cell protection and near-infrared photodynamic application. *Sci. Bull.* 65, 1580–1586.
- Das, B., Dadhich, P., Pal, P., Srivas, P.K., Bankoti, K., Dhara, S., 2014. Carbon nanodots from date molasses: new nanolights for the *in vitro* scavenging of reactive oxygen species. *J. Mater. Chem. B* 2, 6839–6847.
- Deng, H., Zhou, Z., Yang, W., Lin, L.-S., Wang, S., Niu, G., Song, J., Chen, X., 2020. Endoplasmic reticulum targeting to amplify immunogenic cell death for cancer immunotherapy. *Nano Lett.* 20, 1928–1933.
- Dickinson, B.C., Chang, C.J., 2011. Chemistry and biology of reactive oxygen species in signaling or stress responses. *Nat. Chem. Biol.* 7, 504.
- Du, F., Guo, Z., Cheng, Z., Kremer, M., Shuang, S., Liu, Y., Dong, C., 2020. Facile synthesis of ultrahigh fluorescence N, S-self-doped carbon nanodots and their multiple applications for H₂S sensing, bioimaging in live cells and zebrafish, and anti-counterfeiting. *Nanoscale* 12, 20482–20490.
- Gong, G.-F., Chen, Y.-Y., Zhang, Y.-M., Fan, Y.-Q., Zhou, Q., Yang, H.-L., Zhang, Q.-P., Yao, H., Wei, T.-B., Lin, Q., 2019. A novel bis-component AIE smart gel with high selectivity and sensitivity to detect CN⁻, Fe³⁺ and H₂PO₄⁻. *Soft Matter* 15, 6348–6352.
- Gong, Y., Yu, B., Yang, W., Zhang, X., 2016. Phosphorus, and nitrogen co-doped carbon dots as a fluorescent probe for real-time measurement of reactive oxygen and nitrogen species inside macrophages. *Biosens. Bioelectron.* 79, 822–828.
- Hou, J.-T., Yu, K.-K., Sunwoo, K., Kim, W.Y., Koo, S., Wang, J., Ren, W.X., Wang, S., Yu, X.-Q., Kim, J.S., 2020. Fluorescent imaging of reactive oxygen and nitrogen species associated with pathophysiological processes. *Chem* 6, 832–866.
- Huang, H., Lou, X., Hu, B., Zhou, Z., Chen, J., Tian, Y., 2019. A comprehensive study on the generation of reactive oxygen species in Cu-Aβ-catalyzed redox processes. *Free Radic. Biol. Med.* 135, 125–131.
- Huang, H., Tian, Y., 2018. A ratiometric fluorescent probe for bioimaging and biosensing of HBrO in mitochondria upon oxidative stress. *Chem. Commun.* 54, 12198–12201.
- Huang, H., Shen, Z., Chen, B., Wang, X., Xia, Q., Ge, Z., Wang, Y., Li, X., 2020. Selenium-doped two-photon fluorescent carbon nanodots for in-situ free radical scavenging in mitochondria. *J. Colloid Interf. Sci.* 567, 402–409.
- Huang, H., Li, S., Chen, B., Wang, Y., Shen, Z., Qiu, M., Pan, H., Wang, W., Wang, Y., Li, X., 2022. Endoplasmic reticulum-targeted polymer dots encapsulated with ultrasonic synthesized near-infrared carbon nanodots and their application for *in vivo* monitoring of Cu²⁺. *J. Colloid Interf. Sci.* 627, 705–715.

- Huang, H., Chen, B., Li, L., Wang, Y., Shen, Z., Wang, Y., Li, X., 2022. A two-photon fluorescence probe with endoplasmic reticulum targeting ability for turn-on sensing photosensitized singlet oxygen in living cells and brain tissues. *Talanta* 237, 122963.
- Li, H., He, X., Kang, Z., Huang, H., Liu, Y., Liu, J., Lian, S., Tsang, C.H.A., Yang, X., Lee, S.T., 2010. Water-soluble fluorescent carbon quantum dots and photocatalyst design. *Angew. Chem. Int. Edit.* 49, 4430–4434.
- Li, F., Li, T., Sun, C., Xia, J., Jiao, Y., Xu, H., 2017. Selenium-doped carbon quantum dots for free-radical scavenging. *Angew. Chem. Int. Ed.* 56, 9910–9914.
- Li, F., Li, Y., Yang, X., Han, X., Jiao, Y., Wei, T., Yang, D., Xu, H., Nie, G., 2018. Highly fluorescent chiral N-S-doped carbon dots from cysteine: affecting cellular energy metabolism. *Angew. Chem. Int. Edit.* 57, 2377–2382.
- Li, H., Ma, H., 2018. New progress in spectroscopic probes for reactive oxygen species. *J. Anal. Test.* 2, 2–19.
- Li, L., Shi, L., Jia, J., Eltayeb, O., Lu, W., Tang, Y., Dong, C., Shuang, S., 2020. Dual photoluminescence emission carbon dots for ratiometric fluorescent GSH sensing and cancer cell recognition. *ACS Appl. Mater. Interfaces* 12, 18250–18257.
- Li, F., Yang, D., Xu, H., 2019. Non-metal-heteroatom-doped carbon dots: synthesis and properties. *Chem. Eur. J.* 25, 1165–1176.
- Li, K., Yang, J., Gu, J., 2021. Spatially organized functional bioreactors in nanoscale mesoporous MOFs for cascade scavenging of intracellular ROS. *Chem. Mater.* 33, 2198–2205.
- Liu, Y., Duan, W., Song, W., Liu, J., Ren, C., Wu, J., Liu, D., Chen, H., 2017. Red emission B, N, S-co-doped carbon dots for colorimetric and fluorescent dual mode detection of Fe^{3+} ions in complex biological fluids and living cells. *ACS Appl. Mater. Interfaces* 9, 12663–12672.
- Liu, J., Geng, Y., Li, D., Yao, H., Huo, Z., Li, Y., Zhang, K., Zhu, S., Wei, H., Xu, W., Jiang, J., Yang, B., 2020. Deep red emissive carbonized polymer dots with unprecedented narrow full width at half maximum. *Adv. Mater.* 32, 1906641.
- Liu, Y., Jiang, L., Tian, Y., Xu, Z., Wang, W., Qiu, M., Wang, H., Li, X., Zhu, G., Wang, Y., 2023. Covalent organic framework/g- C_3N_4 van der Waals heterojunction toward H_2 production. *Inorg. Chem.* 62, 3271–3277.
- Liu, Z., Tian, Y., 2021. Recent advances in development of devices and probes for sensing and imaging in the brain. *Sci. China Chem.* 64, 915–931.
- Liu, Z., Zhang, Z., Liu, Y., Mei, Y., Feng, E., Liu, Y., Zheng, T., Chen, J., Zhang, S., Tian, Y., 2022. Raman fiber photometry for understanding mitochondrial superoxide burst and extracellular calcium ion influx upon acute hypoxia in the brain of freely moving animals. *Angew. Chem. Int. Ed.* 61, e202111630.
- Liu, Z., Zhu, Y., Zhang, L., Jiang, W., Liu, Y., Tang, Q., Cai, X., Li, J., LH, W., Tao, C., Yin, X., Li, X., Hou, S., Jiang, D., Liu, K., Zhou, X., Zhang, H., Liu, M., Fan, C., Tian, Y., 2023. Structural and functional imaging of brains. *Sci. China Chem.* 66, 324–366.
- Lu, S., Sui, L., Liu, J., Zhu, S., Chen, A., Jin, M., Yang, B., 2017. Near-infrared photoluminescent polymer-carbon nanodots with two-photon fluorescence. *Adv. Mater.* 29, 1603443.
- Lu, D., Tang, Y., Gao, J., Wang, Q., 2018. Concentrated solar irradiation protocols for the efficient synthesis of tri-color emissive carbon dots and photophysical studies. *J. Mater. Chem. C* 6, 13013–13022.
- Luo, W., Wang, Y., Lin, F., Liu, Y., Gu, R., Liu, W., Xiao, C., 2020. Selenium-doped carbon quantum dots efficiently ameliorate secondary spinal cord injury via scavenging reactive oxygen species. *Int. J. Nanomedicine* 15, 10113–10125.
- Rosenkrans, Z.T., Sun, T., Jiang, D., Chen, W., Barnhart, T.E., Zhang, Z., Ferreira, C.A., Wang, X., Engle, J.W., Huang, P., Cai, W., 2020. Selenium-doped carbon quantum dots act as broad-spectrum antioxidants for acute kidney injury management. *Adv. Sci.* 7, 2000420.
- Wang, Y., Hu, A., 2014. Carbon quantum dots: synthesis, properties and applications. *J. Mater. Chem. C* 2, 6921–6939.
- Wang, M., Kaufman, R.J., 2014. The impact of the endoplasmic reticulum protein-folding environment on cancer development. *Nat. Rev. Cancer* 14, 581–597.
- Wang, B., Wang, S., Wang, Y., Lv, Y., Wu, H., Ma, X., Tan, M., 2016. Highly fluorescent carbon dots for visible sensing of doxorubicin release based on efficient nanosurface energy transfer. *Biotechnol. Lett.* 38, 191–201.
- Wang, B., Song, H., Qu, X., Chang, J., Yang, B., Lu, S., 2021. Carbon dots as a new class of nanomedicines: opportunities and challenges. *Coordin. Chem. Rev.* 442, 214010.
- Wei, Z., Liang, P., Xie, J., Song, C., Tang, C., Wang, Y., Yin, X., Cai, Y., Han, W., Dong, X., 2019. Carrier-free nano-integrated strategy for synergetic cancer anti-angiogenic therapy and phototherapy. *Chem. Sci.* 10, 2778–2784.
- Xiao, H., Wu, C., Li, P., Tang, B., 2018. Simultaneous fluorescence visualization of endoplasmic reticulum superoxide anion and polarity in myocardial cells and tissue. *Anal. Chem.* 90, 6081–6088.
- Xie, J., Wang, C., Wang, N., Zhu, S., Mei, L., Zhang, X., Yong, Y., Li, L., Chen, C., Huang, C., Gu, Z., Li, Y., Zhao, Y., 2020. Graphdiyne nanoradioprotector with efficient free radical scavenging ability for mitigating radiation-induced gastrointestinal tract damage. *Biomaterials* 244, 119940.
- Zhang, W., Chavez, J., Zeng, Z., Bloom, B., Sheardy, A., Ji, Z., Yin, Z., Waldeck, D.H., Jia, Z., Wei, J., 2018. Antioxidant capacity of nitrogen and sulfur codoped carbon nanodots. *ACS Appl. Nano Mater.* 1, 2699–2708.
- Zhang, J., Fu, Y., Yang, P., Liu, X., Li, Y., Gu, Z., 2020. ROS scavenging biopolymers for anti-inflammatory diseases: classification and formulation. *Adv. Mater. Interfaces* 7, 2000632.
- Zhang, D.-Y., Liu, H., Li, C., Younis, M.R., Lei, S., Yang, C., Lin, J., Li, Z., Huang, P., 2020. Ceria nanozymes with preferential renal uptake for acute kidney injury alleviation. *ACS Appl. Mater. Interfaces* 12, 56830–56838.
- Zhang, Y., Ma, Z., Zhang, Y., Li, B., Feng, M., Zhao, Y., An, Q., 2021. Biofriendly molecular and protein release substrate with integrated piezoelectric motivation and anti-oxidative stress capabilities. *Nanoscale* 13, 8481–8489.
- Zhang, D.-Y., Younis, M.R., Liu, H., Lei, S., Wan, Y., Qu, J., Lin, J., Huang, P., 2021. Multi-enzyme mimetic ultrasmall iridium nanozymes as reactive oxygen/nitrogen species scavengers for acute kidney injury management. *Biomaterials* 271, 120706.
- Zhao, X., Li, J., Liu, D., Yang, M., Wang, W., Zhu, S., Yang, B., 2020. Self-enhanced carbonized polymer dots for selective visualization of lysosomes and real-time apoptosis monitoring. *iScience* 23, 100982.
- Zhao, Y., Ou, C., Yu, J., Zhang, Y., Song, H., Zhai, Y., Tang, Z., Lu, S., 2021. Facile synthesis of water-stable multicolor carbonized polymer dots from a single unconjugated glucose for engineering white light-emitting diodes with a high color rendering index. *ACS Appl. Mater. Interfaces* 13, 30098–30105.
- Zhen, X., Pu, K., 2018. Development of optical nanoprobe for molecular imaging of reactive oxygen and nitrogen species. *Nano Res.* 11, 5258–5280.
- Zhou, D., Huang, H., Yu, J., Hu, Z., 2021. Lysosome-targetable selenium-doped carbon nanodots for in situ scavenging free radicals in living cells and mice. *Microchim. Acta* 188, 223.
- Zhou, J., Zhou, H., Tang, J., Deng, S., Yan, F., Li, W., Qu, M., 2017. Carbon dots doped with heteroatoms for fluorescent bioimaging: a review. *Microchim. Acta* 184, 343–368.